Control of cellular separation using adaptive surfaces

Michael G. C. Garland, Matthew Santer and Jonathan F. Morrison[a]

Department of Aeronautics, Imperial College, London SW7 2AZ, UK

[a]*j.morrison@imperial.ac.uk*

Abstract

We report results from an experimental investigation of the three-dimensional separation produced by a high-lift aerofoil at moderate incidence, with constant section, where the separation is controlled by the implementation of an adaptive surface. Mean and time-resolved measurements are made using a NASA GA(W)-1 aerofoil with $AR = 6$ at $Re_c = 3.5 \times 10^5$. Surface oil visualisation and stereo Particle Image Velocimetry (PIV) are used to explore the flow field. The mean topology of the flow identifies characteristic spanwise periodic behaviour, "stall cells", along the surface of the model. Analysis of the time-dependent surface pressure shows two distinct frequencies within the flow field. The higher frequency appears at a Strouhal number, $St \approx 0.2$, representative of vortex shedding, and the typical von Kármán vortex street. The lower frequency appears at $St \approx 0.02$, observed as a global fluctuation in stall-cell extent. This lower frequency is apparent in many separated flows, but in the present context, appears to have received only little attention. It correlates with widely observed low-frequency unsteadiness in the wing loading around stall. While this mode is analogous to that observed in other types of separation, here the streamwise extent of the separation varies because the flow is separating from a curved surface rather than from a sharp edge; the width of the separated region also varies. We show that fully-reversible point actuations of an actuated surface with auxetic structure, introduced immediately upstream of the saddle point at the leading edge of the stall cell, reduce the extent of the separated region.

Keywords: separation; stall cell; adaptive surface; auxetic lattice

1. Introduction

Separation is a key limitation in aerofoil performance and hence its understanding and control are of particular interest. Despite this, investigation of the mechanisms leading to separation from an aerofoil are not well understood, and this is essential for effective control. For high Reynolds number aerofoils with predominantly turbulent boundary layers, separation first occurs near the trailing edge and the separation point proceeds upstream with increasing incidence (Mulleners et al., 2008). During an investigation into the flow of a pitching aerofoil around stall conditions, Moss and Murdin (1971) found that, even in a stable air flow, it was not possible to obtain a steady separation pattern. Further investigation identified local regions of detached flow, the bounds of which were observed to be counter-rotating vortices. These induced upwash within the separated region and downwash on the exterior, thus forming a self-stabilising "stall cell".

Gregory et al. (1971) have investigated aerofoil separation and reported that, with changing incidence, α, or Aspect Ratio (AR), the three-dimensional separation pattern varied and was

independent of corner effects from the model endplates. They were also the first to note the existence, under some conditions, of multiple cells on the model surface. Winkelmann and Barlow (1980) extended the data to cover a much larger range of AR and found that the size of stall cell was independent of aspect ratio. Instead, it was observed that, with increasing AR, the number of stall cells present under the same conditions increased with integer increments, as subsequently confirmed by Weihs and Katz (1983). Additionally, it was noted that as incidence increases, the cells merge until, at a sufficient angle, only one cell remains spanning the entire wing planform. The dependence of cell size and distribution on incidence angle was demonstrated experimentally by Boiko et al. (1996). Both Winkelmann and Barlow (1980) and Boiko et al. (1996) mention a state that exists within the incidence range between two stable cell patterns where the cells 'jostle' each other and the global topology switches between integer states. The cause of this behaviour is unknown. However it is clear that it would form the source of further unsteadiness within the flow field with an obvious effect on wing loading also.

The effect of downwash between stall cells predicted by Moss and Murdin (1971) was observed in the behaviour of the surface pressure during experiment by Yon and Katz (1998): surface pressure from the attached flow between stall cells was found to be comparable to the potential flow solution for the same aerofoil at lower angles of attack. Yon and Katz therefore proposed a stall-cell model in which the vortices associated with the counter-rotating foci leave the wing and trail downstream confirming the effective incidence observed experimentally.

Manolesos and Voutsinas (2014) studied the structure of stall cells using a combination of RANS simulations and stereo PIV. To facilitate the experimental study of the flow topology, the authors applied a local perturbation at the spanwise centreline, just downstream of the leading edge forcing the separation pattern to that of a single stall cell. A good correlation between the experimental and computational results is reported. In the computational study, a pair of trailing vortices was identified which partially support the flow model presented by Yon and Katz (1998). In addition to these, the vortex associated with the recirculating region is seen to extend across the entire span and not only within the stall cells. The position of this vortex, and hence the separation line also, change along the span. It is concluded that the distorted path of this vortex relative to the model induces the surface-normal vorticies which bound stall cells.

Zaman et al. (1989) investigated a three-dimensional separation using a series of smoke patterns. A low-frequency 'flapping' of the separated region was observed as well as the expected periodic shedding of vorticity. While trying to isolate the cause of the low-frequency phenomenon, many of the possible sources of oscillation (blower instability, structural resonance, or standing acoustic wave), were discounted. This work also identified that the disturbance was not apparent in flows with a leading-edge separation and only present for a small range of incidence around stall onset in flows which separated from the trailing edge. Yon and Katz (1998) proposed a connection between these disturbances and stall cells in their work outlined above. In flow regimes where stall cells are observed, an unexplained oscillation is also observed although for some experiments at a higher frequency than reported by Zaman et al. (1989) with $St \approx 0.04 - 0.1$. This corresponds to the fan forcing frequency in their experiment and the authors conclude that, while the disturbance may be due to a natural instability of the wake, it is also subject to external forcing. There are many examples of low-frequency flapping in turbulent flow over a backward-facing step (e.g. Heenan and Morrison, 1998).

Here, we report the results of experimental tests highlighting some key characteristics of stall cells generated by a turbulent separation. Rodríguez and Theofilis (2011) show that, at low Reynolds numbers $Re \approx 200$, the surface streamlines generated by the dominant stationary global mode of laminar separation are very similar to stall cells in both laminar and turbulent

flow. It is interesting to note that Hunt et al. (1978) and Foss (2004) describe the topological rules governing their behaviour.

Here, we show how the stall cell topography may be affected by the actuation of deployable vortex generators leading to a technique for separation control. In this, we take our inspiration from the observation by Wu and Wu (1996) that control is possible where vorticity flux is generated locally by a surface to improve its global distribution. As described by previous authors, important local regions are critical points in the skin-friction pattern, notably saddle points at which the separating stream surface is formed only by those streamlines initiating from these points.

A useful expression that relates the generation of surface flux, $\boldsymbol{\sigma}$ of vorticity $\boldsymbol{\omega}$, to the time-dependent details of the surface geometry is given by

$$\boldsymbol{\sigma} = -\nu(\mathbf{n}.\nabla\boldsymbol{\omega})_{\mathrm{w}} = -\boldsymbol{n}\times\boldsymbol{a} - \boldsymbol{n}\times\frac{\nabla p}{\rho} + \left(\boldsymbol{n}\times\frac{\tau_{\mathrm{w}}}{\rho}\right)\cdot\nabla_{\pi}\boldsymbol{n} - \boldsymbol{n}\left(\boldsymbol{n}\cdot\left(\nabla\times\frac{\tau_{\mathrm{w}}}{\rho}\right)\right), \tag{1}$$

where $\boldsymbol{n}$ is the outward pointing unit-normal vector and $\nabla_{\pi}\boldsymbol{n}$ is the tangential component of the nabla operator (Wu and Wu, 1996). The first three terms on the right-hand side ("ascending mechanisms of tangential vorticity") represent, respectively, the effects of surface acceleration, $\boldsymbol{a}$, pressure gradients and curvature. These, together with the last term representing the generation of surface-normal vorticity through the action of viscous diffusion, are all strongly coupled. In particular, equation (1) suggests how time-dependent surface motion can be effective, even when the time-mean displacement is zero. It also shows how sharp edges in the surface (as in the case of conventional vortex generators) are particularly effective when the curvature term is infinite. In the context of time-dependent surface deformation, equation (1) is discussed further by Dearing et al. (2007).

2. Experimental Setup

The experiments are conducted in a closed-circuit wind tunnel with a working section of 1.38 m $\times$ 1.22 m $\times$ 3.0 m with a contraction ratio of 4.92 : 1. The air is driven by a four-bladed fan with a maximum free-stream velocity of approximately 40 ms^{-1}. The free-stream turbulence intensity is less than 0.1% at 25 ms^{-1}. The wing has constant cross section of an unswept NASA GA(W)-1 aerofoil (McGhee and Beasley, 1973). This is a sub-critical, high-lift aerofoil which has been shown to exhibit 3D separation in previous research (Flynn et al., 2001). Previous experimental studies (Winkelmann and Barlow (1980); Yon and Katz (1998)) indicate that a stable pattern of stall cells is observed for aspect ratios $6 < AR < 9$, giving three stable cells, two complete ones with a half-cell at either end.

To maximise the chord Reynolds number, a chord of 0.22 m was chosen. At $U_{\infty} = 24.5$ ms^{-1}, $Re_c \approx 3.5\times10^5$. Endplates are used to remove the effect of the tunnel-wall boundary layers, and a span of 1.32 m was selected giving $AR = 6$. The maximum blockage at $\alpha = 20^{\circ}$ is approximately 6%. The wing is suspended from a drag balance in the roof of the tunnel. The mechanical nature of the drag balance makes it unsuitable for measuring the unsteady forces generated by separation. However, it does provide a suitable rigid mounting point for the model: it is mounted upside-down to allow laser access through optical-quality glass panels in the floor and side wall. The boundary layer is tripped at $x/c = 0.04$ using glass ballotini of diameter $0.4 < d < 0.8$ mm.

Surface pressure measurements are made using a number of Chell μDAQs, of range of ±1 kPa with thermal compensation. For the 32 channel transducers used here, the maximum sampling

rate per channel is 625 /s. All pressures were therefore sampled at 500 Hz to avoid data loss. The surface tappings are connected to the transducer by 0.97 m lengths of 0.5 mm diameter plastic tubing running through the model. Attenuation is calibrated by dynamic forcing and compared to ouput of an Endevco 8507C-1 piezoresistive pressure transducer located within the tapping array. At low frequencies, the phase shift was neligible.

The PIV laser, cameras and optics are mounted on a 3-stage linear traverse. Once aligned, this allows the light sheet and cameras to move in the same frame of reference. This enables recording of data from planes near to the model for which it would otherwise not be possible to obtain an accurate calibration. The PIV equipment was used in two arrangements to obtain different fields of view. The light sheet may enter either through the side wall, parallel to the model, with cameras arranged underneath the tunnel as shown in figure 1, or through the tunnel floor, perpendicular to the model chord, with cameras mounted on either side of the working section. The overlapping field of view for the cameras is 178.6×133.7 mm (spanwise $\times$ streamwise) and each 32×32 interrogation window corresponds to 1.1×1.1 mm.

The coordinate system for the wing is defined by the streamwise direction $0 \leq x/c \leq 1$, with the surface normal, y and the spanwise direction where $z = 0$ corresponds to the wing centre-line.

2.1. Auxetic lattice surface

The wing model is fabricated with recesses to enable the insertion of the adaptive surface module which is $\Delta x/c = 0.38$ in length and $\Delta z/c = 0.41$ wide, with its leading edge at $x/c = 0.086$ and its centre-line aligned with that of the wing. The module may be freely moved in the spanwise direction to enable its positioning directly upstream of a stall cell saddle point, (x_s, z_s). For the present results, we consider a saddle point at $x_s/c = 0.30, z_s/c = -1.06$ (inboard of the wing centre-line). Under the effect of a single, controlled out-of-plane displacement, the surface is deformed elastically to produce a protruding bump which acts as a vortex generator. An ideal non-deployable vortex generator has a sharp profile which may not be achieved through actuation of a compliant surface. The deformed shape of a deployable vortex generator is additionally limited by the curvature that may be elastically sustained by the surface structure. A deployed surface with non-zero Gaussian curvature is required which may only be attained from a continuous compliant surface via the action of in-plane (membrane) strains. This places significant limitations on the out-of-plane deformation that can be achieved before material limits, such as yield strength, are reached.

Use of a lattice structure provides an effective means to mitigate this problem. Global bending stiffness – which is necessary for the structure to perform effectively as an aerodynamic skin – is retained. However, the membrane strains resulting from out-of-plane deformation of the continuous surface are replaced by localized bending of the thin lattice members which enables significantly greater deformation before material limits are reached. In order to maximize further the amenability of the surface to out-of-plane deformation, an auxetic (negative Poisson's ratio) lattice structure having an hexagonal chiral geometry is adopted.

Owing to the recognition that discontinuous surface changes cannot be achieved through flexure-based morphing, an optimization study has been carried out to determine the hexagonal chiral lattice geometry and appropriate boundary conditions that achieves the best performance. The surface deformation was optimised by using large-eddy simulation of the boundary layer development with the shape factor as the objective function. Its minimisation results in a turbulent flow that is resistant to separation. In addition, a constraint is specified such that the stress in the structure is less than the yield strength of stainless steel. The resulting design is the optimal

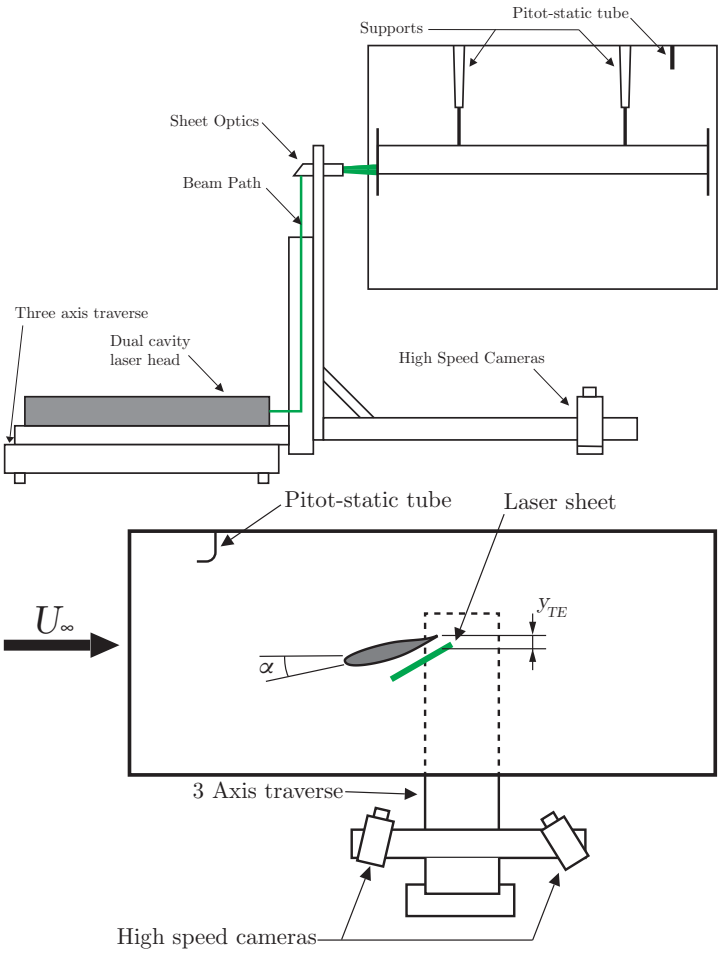

Figure 1: Setup of the GA(W)-1 wing: top, downstream view; bottom, side view.

compromise between an effective vortex generator and retaining the ability to deploy and retract elastically. Full details of the design optimization procedure may be found in Garland (2016); Garland et al. (2017).

A fabricated adaptive surface module is shown in Figure 2a. The auxetic lattice is micromachined from stainless steel, and encased in a thin layer of silicone to form an air-tight aerodynamic surface. Details of the manufacturing process have previously been reported by Garland et al. (2017). The surface deformation under actuation is determined using a Faro Arm laser scanner. A surface fitted to the resulting point cloud data is shown in Figure 2b. Cross-sections of the deformed surface through the point of highest deformation ($x/c = 0.25,\ z/c = 0.0$) are shown in Figures 2c and d. The regions of large curvature enabled by the auxetic lattice structure are clear. The figures also show the surface deformation when actuation is removed. It can be seen that

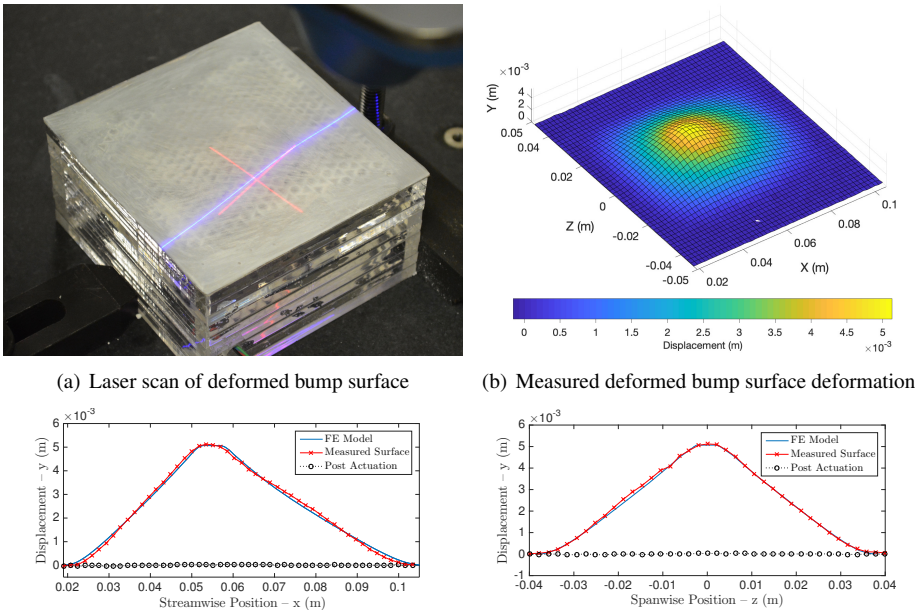

(a) Laser scan of deformed bump surface

(b) Measured deformed bump surface deformation

(c) Streamwise lattice deformation

(d) Spanwise lattice deformation

Figure 2: Fabrication and measurement of active auxetic deployable lattice

the surface returns to flat and that the deformation is fully elastic. The surface may therefore be repeatedly deployed and retracted as required. Actuation of the structure is implemented using a linear actuator driven by a stepper motor. The motor is driven with a micro-stepping driver giving a positional accuracy of $\pm$ 0.20μm. Further details are given by Garland (2016); Garland et al. (2017).

3. Results

3.1. Unmodified flow

3.1.1. Surface skin friction

For a qualitative assessment of the skin-friction lines on the wing suction surface, oil flow visualisation was conducted at a range of incidences. The experiment was run at a free-stream velocity of 25 ms^{-1} and the chosen incidence angle until the paraffin evaporated, fixing the skin-friction patterns. Figure 3 shows a typical series of surface flow patterns observed over the partially-stalled incidence range. The critical points have been marked, along with the local flow directions, in each image based on the observations made during of a number of experiments. A repeating series, consisting of two saddle points (marked S) and two counter-rotating foci (marked F), is observed at each incidence, indicating a periodic array of stall cells. In the regions between the Focus-Saddle-Focus structures, the undisturbed oil flow pattern is seen to continue farther along the chord toward the trailing edge than in the vicinity of the saddle point. This is particularly evident in figure 3(e) but can be observed in all cases and is indicative of regions of

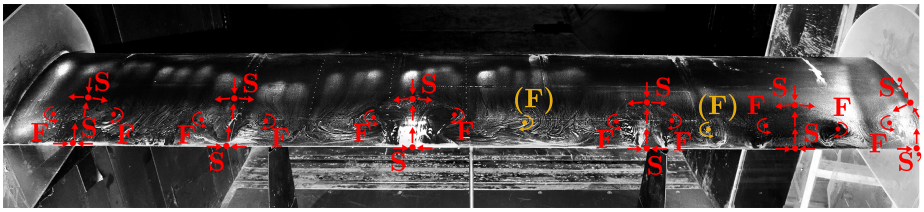

(a) 12°

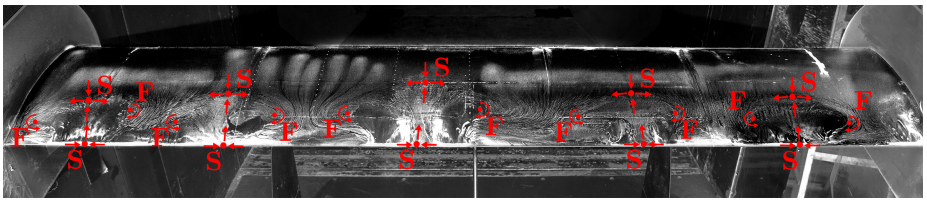

(b) 14°

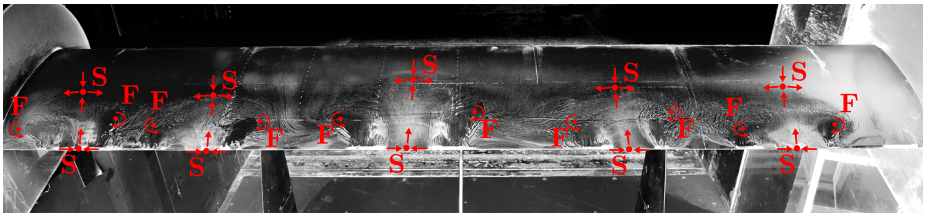

(c) 15°

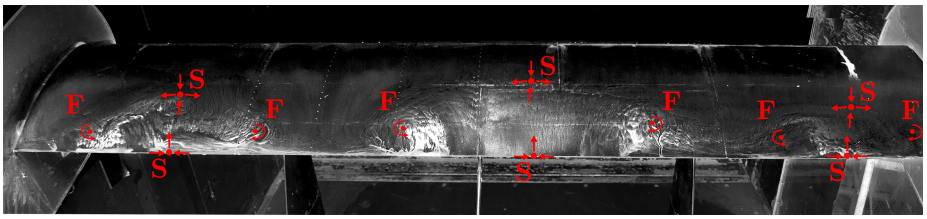

(d) 16°

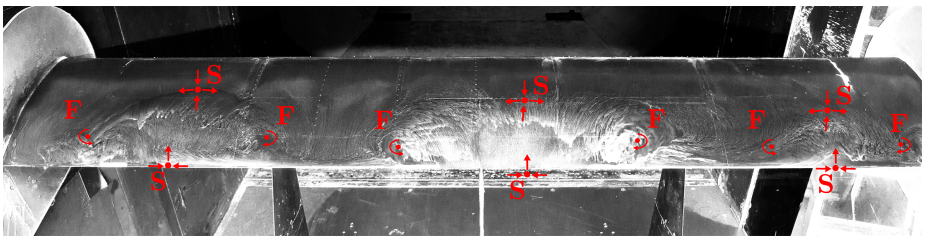

(e) 17°

Figure 3: Surface oil flow visualisation of the wall shear stress distribution for a NASA GA(W)-1 aerofoil at $Re_c \approx 3.5 \times 10^5$. Critical points are over-layed and distinguished between Saddles – S, and Foci – F.

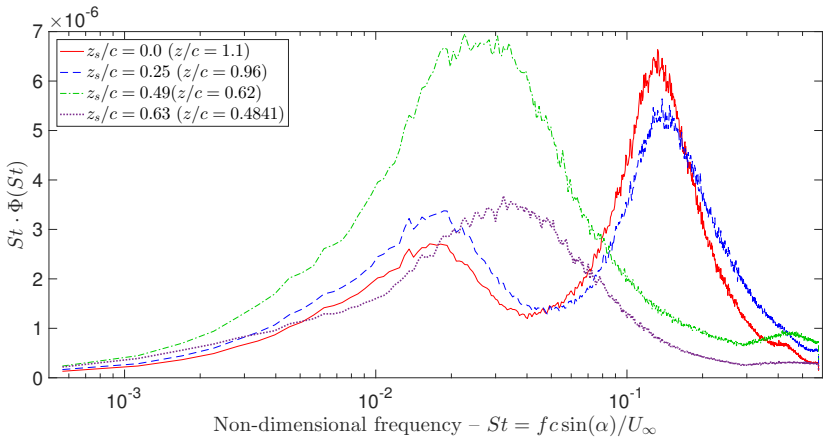

Figure 4: Surface pressure spectra from four spanwise positions across a stall cell, $Re = 3.5 \times 10^5$ and $\alpha = 15°$.

attached flow between the cells. As reported by previous authors, the separated area within each cell is seen to increase with incidence angle.

At $\alpha = 12°$ and $16°$, the stall-cell positions were observed to switch between two stable states during a single run. Both states are repeatable and spatially offset by approximately half of the spanwise period. No characteristic time period was observed with each layout remaining steady for between approximately 2 – 30 seconds before switching to the alternative topology. This is shown in figure 3(a) by the isolated foci (marked in yellow) visible in the oil flow pattern.

3.1.2. Surface pressure spectra

Figure 4 shows the pre-multiplied energy spectra $St \cdot \Phi(St)$ of surface pressure fluctuations against the corresponding Strouhal number, $St = fc\sin(\alpha)/U_\infty$, where the mean-square pressure is given by

$$\overline{p^2} = \int_0^\infty St\,\Phi(St)\,\mathrm{d}(\log St). \tag{2}$$

Data are presented from four spanwise positions with constant chordwise location $x/c = 0.74$, where $z_s = 0$ is the line of symmetry of the stall cell. The surface pressure was sampled at 500 Hz for 3600 s and is normalised by the free-stream dynamic pressure.

While the surface pressure varies little throughout the separated region, the spectral density of the fluctuating component can be seen to vary between two distinct frequency ranges. At the centre of the cell, $z_s/c = 0$, a high-energy oscillation can be seen at frequency $St \approx 0.16$, the anticipated frequency range for von Kármán type vortex shedding. An additional oscillation is visible at a frequency an order of magnitude lower at $St \approx 0.02$, with a significantly lower amplitude.

At measurement locations close to the edges of the cell, the magnitude of the peak at the shedding frequency decreases while that of the second, lower frequency, oscillation is seen to grow. At $z_s/c = 0.49$, the high frequency oscillation is no longer distinguishable while that at the lower frequency grows significantly. At $z_s/c = 0.63$, beyond the time-mean extent of the cell, the overall levels of fluctuation are reduced but a broad, low-frequency, signal is still visible in the spectrum. The presence of both signals within the pressure time-history at two widely separated

frequencies and with varying amplitudes at $z_s/c = 0.0$ and at 0.25 indicates that the two features are independent of one another. The lower-frequency behaviour also appears in time sequences of the PIV reconstructions in the $(x, z)-$plane. We deduce therefore that the lower frequency is due to a wholesale expansion/contraction of the stall cell in that plane, rather than a meandering of the whole stall cell.

3.1.3. Modal decomposition of velocity field

To identify velocity-field features corresponding to the surface-pressure spectra, the fluctuating component of a number of velocity fields is examined by extraction of POD modes. A linear series of coefficients can be found by projecting the POD mode back onto the original vector field. In this way a time series of the relative weights of each mode may be examined in the frequency domain, so that the corresponding spectra may be calculated. The PIV frames and pressure data are sampled at the same frequency so that any features resolved by the pressure data should also be visible in the velocity data. Further details appear in Garland (2016).

Decompositions were conducted on several planes within the flow field: two $(x, y)-$planes, those intersecting the saddle point and wall-normal foci, and one $(x, z)-$plane at $y_{TE} = 20$ mm (see figure 1). Here, data are examined for the first 10 POD modes calculated in the $(x, y)-$plane at $z_s/c = 0$. As expected, the greatest relative modal energy appears in the lowest mode, $m = 1$, for which it is approximately 30%. For higher modes, the relative modal energy decreases from 3% at $m = 2$ to 1% at $m = 6$. Figure 5 shows the detail for the modes, $m = 1$ and then $m = 4, 5, 6$, the more energetic modes. For each, the vorticity distribution of the vector field for each POD mode is shown alongside the spectral content of the POD coefficients. The streamlines corresponding to the mean flow are overlaid on the vorticity contours to provide a visual reference.

In both streamwise/wall-normal planes, the more energetic modes are seen to act over the cell area. The modal coefficients relating to these large coherent variations are seen to occur at non-dimensional frequency $St \sim O(10^{-2})$. The exception to this trend is seen in mode $m = 2$ in plane $z_s/c = 0$ (not shown), where a narrow spike occurs at $St \approx 10^{-1}$. The energy in this mode is located near to the trailing edge of the aerofoil. Examination of the source images indicates that this is due to a fluctuating reflection of the laser sheet from the wing surface.

The energy content for the higher modes is concentrated at higher frequencies, $St \sim O(10^{-1})$. The vector fields forming these modes contain coherent concentrations of vorticity with alternating sign which are significantly smaller than the mean stall cell. These are arranged along the shear layer separating the mean recirculating region and the free-stream. These structures are typical of von Kármán shedding from bluff body wakes and occur in the expected frequency range.

3.2. Separation control with adaptive actuator

Figure 6 shows the '$x-$wise' velocity (in a direction normal to the leading edge of the aerofoil, but in the plane of the light sheet shown in figure 1. In the unactuated case, the position and width of the stall cell compare well with previous measurements. When the device is actuated to the design height, (the same as the vertical displacement of a discontinuous VG), the focus of the stall cell is seen to move towards the saddle point, decreasing the the size of the recirculating region. However, it is also noted that the saddle point moves upstream. This behaviour is attributed to the curvature constraint required by a morphing structure described in Section 2.1. In order to maintain an elastic deformation, the surface curvature must remain finite and continuous.

Without the possibility of a sharp trailing edge on the actuator, the vorticity generated is shed from the device periodically rather than continuously. However, it is clear that the separation has been controlled using a localized deployable vortex generator.

4. Conclusions

We show that three-dimensional (stall-cell) separation from a high-lift aerofoil comprises two discrete frequency ranges, one approximately ten times lower than that normally associated with a vortex-shedding mode. This lower-frequency behaviour appears as an oscillation of the whole stall cell. It is also shown that the stall cells are beneficially affected when the surface is deformed using a point actuator comprising an adaptive device based on an auxetic lattice structure. The adaptive surface is shown to be fully elastic in both deployment and retraction. While less effective than traditional non-retractable vortex generators, such a structure generates no parasitic drag when not required while still providing a degree of separation control.

In order to improve the effectiveness of the deployable vortex generators which retaining the capability to deploy and retract elastically, a number of steps may be considered in further work. Smaller radii of curvature – resulting in deformed shapes closer to an ideal design – may be achieved without permanent plastic deformation via a combination of material selection and structural geometry. Materials with higher yield strain than stainless steel may be adopted, although this would have implications with respect to the ease and accuracy of micromachining.

A potentially effective approach to refining the structure approach would be to add locally more compliant regions in the surface by reducing the lattice depth where required. This would have the effect of permitting much smaller radii of curvature along these compliant hinge lines. Alternative chiral lattice structures with improved auxetic properties are also available. Finally, a change of objective function in the optimization process could also be appropriate in which a structural objective would be coupled with the currently-used aerodynamic objective in order to prioritize sharper shape changes.

Acknowledgements

We are indebted to EPSRC Doctoral Training Account (Grant Number 1256485) for financial support through the Department of Aeronautics.

References

Boiko, A. V., Dovgal, A. V., Zanin, B. Y., Kozlov, V. V., 1996. Three-dimensional structure of separated flows on wings (review). Thermophysics and Aeromechanics 3 (1), 1–13.

Dearing, S. S., Lambert, S., Morrison, J. F., 2007. Flow control with active dimples. Aero. J. 111, 705–714.

Flynn, G. A., Morrison, J. F., Mabey, D. G., 2001. Buffet alleviation on swept and unswept wings at high incidence. J. Aircraft 38 (2), 368–378.

Foss, J. F., 2004. Surface selections and topological constraint evaluations for flow field analyses. Exp. Fluids 37, 883–898.

Garland, M. G. C., 2016. Adaptive structures for the control of celluar separation. Ph.D. thesis, Imperial College London.

Garland, M. G. C., Santer, M. S., Morrison, J. F., 2015. Adaptive vortex generator structures for the reduction of turbulent separation. Tech. Rep. 2015-0266, AIAA.

Garland, M. G. C., Santer, M. S., Morrison, J. F., 2017. Optimal aero-structural design of an adaptive surface for boundary layer motivation using an auxetic lattice skin. J. Int. Material Sys. and Structs. 28, 2414–2427.

Gregory, N., Quincey, V. G., L., O. C., Hall, D. J., 1971. Progress report on observations of three-dimensional flow patterns obtained during stall development on aerofoils, and on the problem of measuring two-dimensional characteristics. Tech. Rep. CP1146, Aeronautical Research Council.

Heenan, A. F., Morrison, J. F., 1998. Passive control of pressure fluctuations generated by separated flow. AIAA J. 36 (6), 1014–1022.

Hunt, J. C. R., Abell, C. J., Peterka, J. A., Woo, H., 1978. Kinematical studies of the flows around free or surface-mounted obstacles; applying topology to flow visualization. J. Fluid Mech., 179–200.

Manolesos, M., Voutsinas, S. G., 2014. Study of a stall cell using stereo particle image velocimetry. Phys. Fluids 26 (4), 045101.

McGhee, R. J., Beasley, W. D., 1973. Low-speed aerodynamic characteristics of a 17-percent-thick medium speed airfoil designed for general aviation applications. Tech. Rep. TN D-7428, NASA.

Moss, G. F., Murdin, P. M., 1971. Two-dimensional low-speed tunnel tests on the NACA 0012 section including measurements made during pitching oscillations at the stall. CP 1145, Aeronautical Research Council.

Mulleners, K., Hemireg, A., Raffel, M., 2008. Investigations of trailing edge stall on 2D airfoils. In: 14th Int. Symposium on Applications of Laser Techniques to Fluid Mechanics.

Rodríguez, D., Theofilis, V., 2011. On the birth of stall cells on airfoils. Theor. Comput. Fluid Dyn. 25, 105–117.

Weihs, D., Katz, J., 1983. Cellular patterns in poststall flow over unswept wings. AIAA Journal 21 (12), 1757–1759.

Winkelmann, A. E., Barlow, J. B., 1980. Flowfiled model for a rectangular planform wing beyond stall. AIAA J. 18 (8), 1006–1008.

Wu, J. Z., Wu, J. M., 1996. Vorticity dynamics on boundaries. Adv. App. Mech. 32, 119–275.

Yon, S. A., Katz, J., 1998. Study of the unsteady flow features on a stalled wing. AIAA J. 36 (3), 305–312.

Zaman, K. B. M. Q., McKinzie, D. J., Rumsey, C. L., 1989. A natural low-frequency oscillation of the flow over an airfoil near stalling conditions. J. Fluid Mech. 202, 403–442.

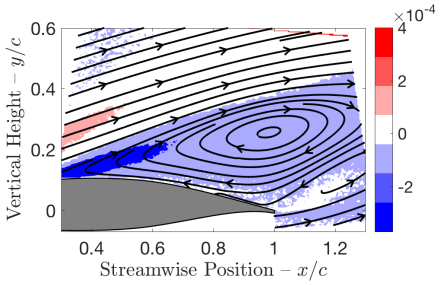

(a) Vorticity distribution $m = 1$

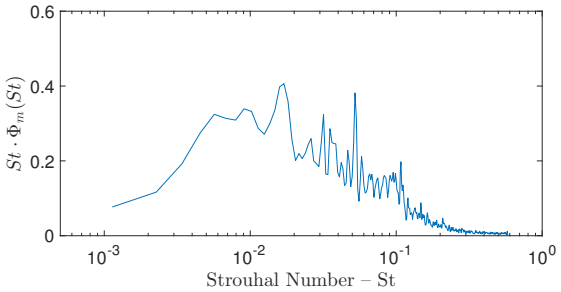

(b) Frequency distribution $m = 1$

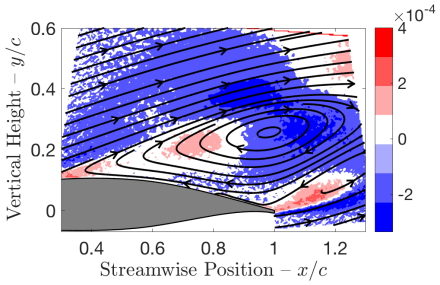

(c) Vorticity distribution $m = 4$

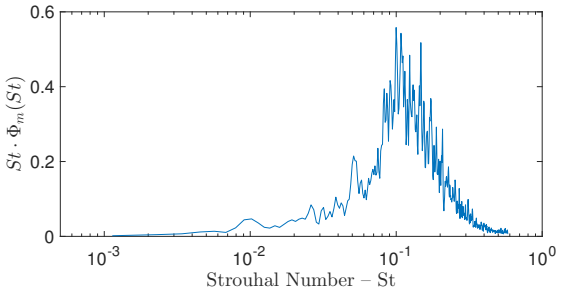

(d) Frequency distribution $m = 4$

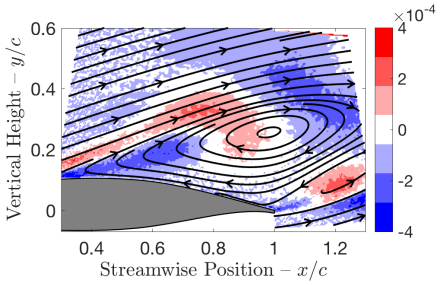

(e) Vorticity distribution $m = 5$

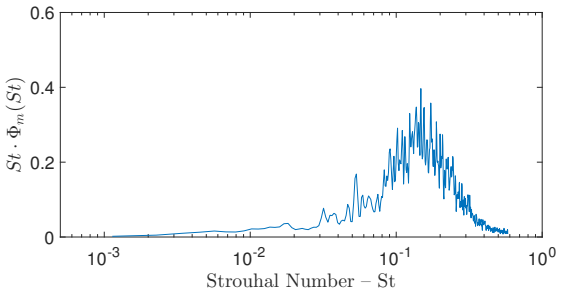

(f) Frequency distribution $m = 5$

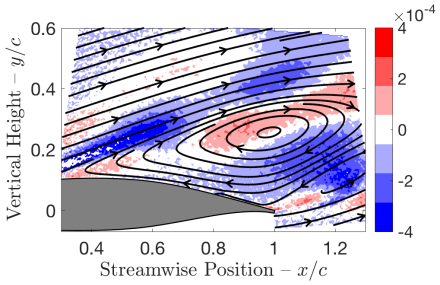

(g) Vorticity distribution $m = 6$

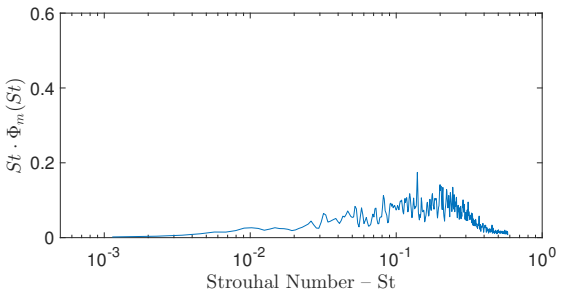

(h) Frequency distribution $m = 6$

Figure 5: POD Modes for $(x, y)-$plane at $z_s/c = 0$.

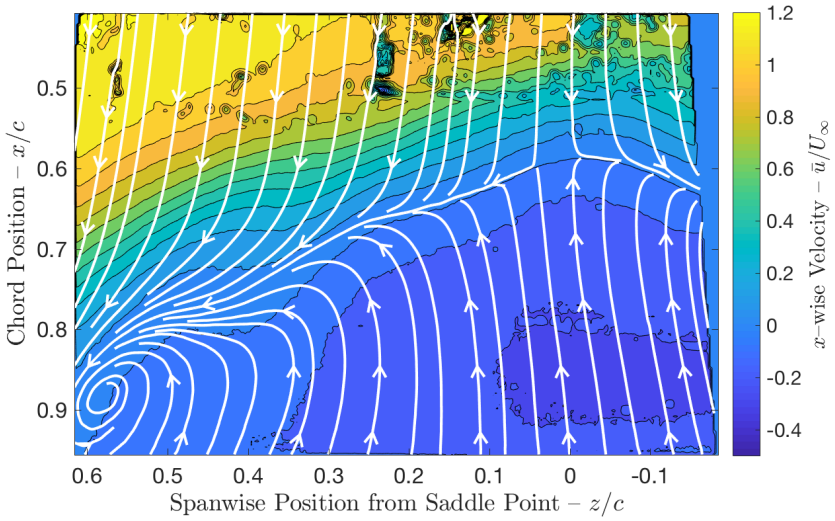

(a) No actuation

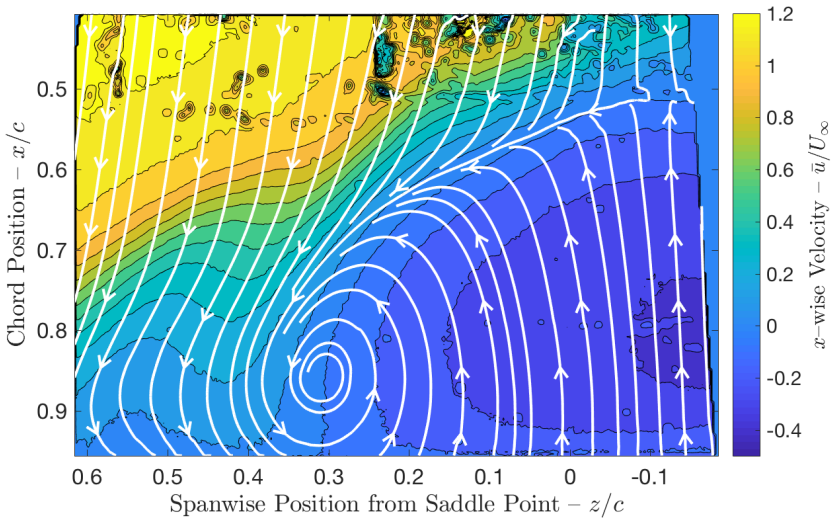

(b) Vertical displacement 2.63 mm

Figure 6: Effect of adaptive VG: contours of in-plane mean $x-$wise velocity.